

Manuscript

Enhanced Phonon-Phonon Interactions and Weakened Electron-Phonon Coupling in Charge-Density-Wave Topological Semimetal EuAl_4 with a Possible Intermediate Electronic State

Shize Cao,^{1,2} Feng Jin,¹ Jianzhou Zhao,³ Yun-Ze Long,^{2,} Jianlin Luo,^{1,4} Qingming Zhang^{1,5}*

and Zhi-Guo Chen^{1,4,}*

¹ Beijing National Laboratory for Condensed Matter Physics, Institute of Physics, Chinese Academy of Sciences, Beijing 100190, China

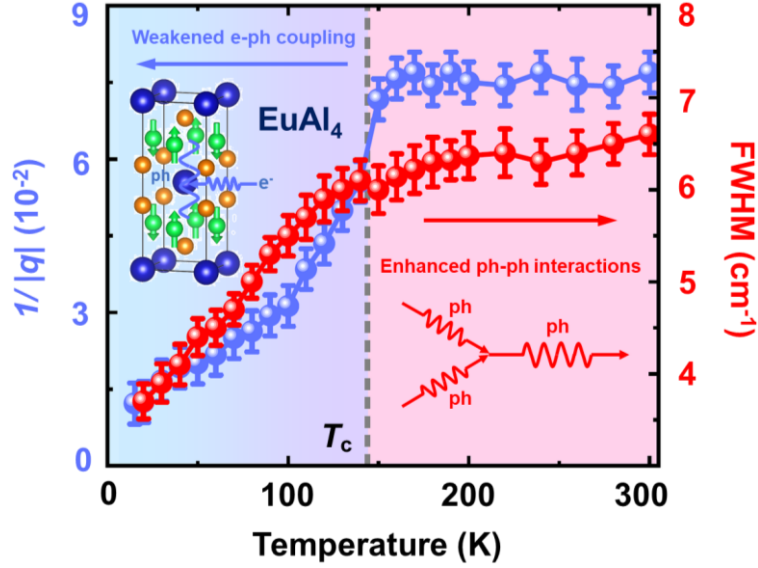
² Collaborative Innovation Center for Nanomaterials & Devices, College of Physics, Qingdao University, Qingdao 266071, China

³ Co-Innovation Center for New Energetic Materials, Southwest University of Science and Technology, Mianyang 621010, China

⁴ Songshan Lake Materials Laboratory, Dongguan, Guangdong, 523808, China

⁵ School of Physical Science and Technology, Lanzhou University, Lanzhou 730000, China

ABSTRACT: The origin of charge density wave (CDW) is a long-term open issue. Furthermore, the evolution of phonon-phonon interactions (PPI) across CDW transitions has rarely been investigated. Besides, whether electron-phonon coupling (EPC) would be weakened or enhanced after CDW transitions is still under debate. Additionally, CDW provides a fertile ground for uncovering intriguing intermediate electronic states. Here, we report a Raman spectroscopy study of the PPI and EPC in topological semimetal EuAl_4 exhibiting a CDW phase below temperature $T_c \sim 145$ K. The free-charge-carrier-density (n_c) and temperature dependences of the Fano asymmetric factors ($1/|q|$) of the two phonon modes A_{1g} and B_{1g} indicates that below T_c , the EPC becomes weakened probably due to the reduction of the n_c . Interestingly, in the temperature range 50—145 K, the steep growth of the $1/|q|$ leading to the significant deviation from the linear dependence on the n_c , together with the shoulder-like features in the temperature evolutions of the $1/|q|$ and the n_c around 50 K, implies the possible existence of an intermediate electronic state with the EPC distinctly larger than the CDW ground state in EuAl_4 . Furthermore, below T_c , the faster decrease in the full width at half maxima of the B_{1g} phonon mode representing the collective vibrations of the CDW-modulated Al^1 atoms suggests that a remarkable growth of the PPI for the B_{1g} phonon mode after the CDW phase transition, which is in contrast to the weakening of the EPC and thus may mainly arise from the strengthening of lattice anharmonicity in EuAl_4 . Our results not only highlight the significance of the enhanced PPI and the weakened EPC in completely understanding the formation of the CDW phase but also initiate the exploration of novel intermediate electronic states in EuAl_4 .



TOC Graphics

Keywords: phonon-phonon interactions, electron-phonon coupling, charge density wave, Topological semimetal, Raman spectroscopy

Charge density wave (CDW), which represents a quantum state of matter with the charge density and underlying lattice periodically modulated, has generated enormous interest in the scientific community because it provides a platform for realizing a variety of quantum phenomena, such as electronic nematic state^[1-4], axion insulator state^[5-6], superconductivity^[7-11] and anomalous Hall effect^[12]. Therein, electronic nematic state, which was revealed to show an intriguing entanglement with unconventional superconductivity^[13-18], is a type of intermediate electronic states adjacent to CDW ground state. Revealing the mechanism of the formation of CDW states is an important step towards not only searching for new CDW materials but also achieving interesting quantum phenomena. However, the driving mechanism for the formation of CDW remains elusive. For one-dimensional systems, the Fermi surface nesting was proposed to cause the divergence of the Lindhard response function, which can result in the presence of CDW order^[19-20]. Nonetheless, since small deviation from perfect

Fermi nesting would greatly suppress the divergence of the Lindhard response function, Fermi-surface-nesting induced CDW were observed in few realistic materials. Many-body interactions including phonon-phonon interactions (PPI) and electron-phonon coupling (EPC) play crucial roles in the emergence of various quantum states in condensed matter^[21-22]. Therein, a sufficiently strong momentum-dependent EPC was suggested to trigger Kohn anomaly (or phonon softening), which can also induce a CDW phase transition^[23]. It is a pity that a consensus on the evolution of the strength of EPC across CDW transitions has not been reached, e.g., the EPC strength decreases in ZrTe_3 ^[24] but increases in $\text{La}_{1.8-x}\text{Eu}_{0.2}\text{Sr}_x\text{CuO}_{4+\delta}$ ^[22] upon entering the CDW state. In addition, the change in the strength of phonon-phonon interactions (PPI) across CDW transitions has rarely been reported^[21].

A rare-earth intermetallic EuAl_4 crystallizes in the centrosymmetric tetragonal structure (the space group $I4/mmm$) with two types of Al atoms— Al^1 and Al^2 . Below a critical temperature $T_c \sim 145$ K, EuAl_4 was revealed to undergo an incommensurate CDW order with the positions of the Al^1 and Eu atoms modulated^[25-30]. Besides, at $T_\chi \sim 10.1$ K in the helical spin-density-wave state of EuAl_4 , a first-order phase transition gives rise to a spontaneous flipping of spin chirality^[31-32]. Moreover, nontrivial topology including topological non-trivial bands in momentum space^[33-34] and topological spin textures—skyrmion in real space was proposed to exist in EuAl_4 ^[35]. Furthermore, topological Hall effect is likely to accompany with the CDW in EuAl_4 ^[36]. Therefore, EuAl_4 can serve as a platform for studying the interplay between CDW and nontrivial topology. Clarifying the microscopic mechanism for the formation of the CDW entangled with nontrivial topology in EuAl_4 would lay a solid foundation for exploring exotic

effects arising from the combination of CDW and nontrivial topology. Previous investigations indicate that the softening of a transverse acoustic phonon mode in EuAl_4 is a crucial driving force for the presence of its CDW order^[37]. Nonetheless, the evolutions of the EPC and PPI across CDW transitions in EuAl_4 , which is expected to offer significant information for completely understanding microscopic mechanism for its CDW formation, were seldom investigated by experiments.

Raman spectroscopy is an efficient experimental technique for probing phonon modes which include the information about PPI and EPC in solids^[21, 24, 38-41]. Thus, a Raman spectroscopy study of the temperature evolutions of the Raman-active phonons across the CDW transition in topological semimetal EuAl_4 , which has yet been performed up to now, would shed light on the evolutions of PPI and EPC. Here, we performed the Raman spectroscopy measurements of the (001) faces of the EuAl_4 single crystals in the temperature range from 15 to 300 K in the backscattering configuration on a Horiba Jobin Yvon LabRAM HR Evolution micro-Raman spectrometer using the 473 nm laser as the light source (see the details about the single-crystal growth, and the X-ray-diffraction characterization in Section 1 of Supporting Information). The EuAl_4 single crystals were cooled using low-temperature helium exchange gas in an AttoDRY 2100 cryostat.

Figure 1a and **1b** depict two asymmetric peak-like features around 247 cm^{-1} and 390 cm^{-1} in the Raman spectra of the EuAl_4 single crystals at different temperatures. To study the nature of the observed peak-like features, we analyzed the $I4/mmm$ space group of its crystal structure.

The phonon modes of EuAl₄ at the Γ point can be decomposed into the following irreducible representations: $[A_{1g} + B_{1g} + 2E_g] + [2A_{2u} + 2E_u] + [A_{2u} + E_u]$, where the first, second, and third terms represent the Raman-active, infrared-active, and the acoustic phonon modes, respectively.

The corresponding Raman tensors of the $I4/mmm$ space group can be expressed as:

$$A_{1g} = \begin{pmatrix} a & 0 & 0 \\ 0 & a & 0 \\ 0 & 0 & b \end{pmatrix} \quad B_{1g} = \begin{pmatrix} c & 0 & 0 \\ 0 & -c & 0 \\ 0 & 0 & 0 \end{pmatrix} \quad (1)$$

$$E_g = \begin{pmatrix} 0 & 0 & 0 \\ 0 & 0 & d \\ 0 & d & 0 \end{pmatrix} \quad E_g = \begin{pmatrix} 0 & 0 & -d \\ 0 & 0 & 0 \\ -d & 0 & 0 \end{pmatrix} \quad (2)$$

where the a , b , c and d are the tensor elements and their values depend on the cross-section of Raman scattering. We further performed *ab initio* calculations of the phonon spectrum of EuAl₄ (see **Figure 2a** and the details about our *ab initio* calculations in Section 1 of Supporting Information). The yellow and green dots in **Figure 2a** indicate that the two phonon bands at the Γ point, which separately host the symmetry B_{1g} and A_{1g} , exhibit the energies: 232.4 cm⁻¹ and 399.4 cm⁻¹. Considering that the energies of the two peak-like features in the measured Raman spectra of the EuAl₄ single crystals are quite close to (i) those of the calculated phonon modes B_{1g} around 232.4 cm⁻¹ and A_{1g} around 399.4 cm⁻¹ of EuAl₄ (see **Table 1**), and (ii) those of the previously reported phonon modes B_{1g} (around 229.7 cm⁻¹) and A_{1g} (around 359.9 cm⁻¹) of its counterpart SrAl₄ with isostructure and isovalence^[34], the asymmetric peak-like features around 247 cm⁻¹ and 390 cm⁻¹ in **Figure 1a** and **1b** can be assigned as the B_{1g} and A_{1g} phonon modes, respectively. Therein, the B_{1g} and A_{1g} phonon modes separately represent the collective vibrations of the Al¹ and Al² atoms (see **Figure 2b** and **2c**).

As is well known, fitting an asymmetric phonon mode using Breit-Wigner-Fano (i.e., BWF) line shape can yield the asymmetric factor $1/|q|$, which quantifies the strength of EPC. To obtain the temperature dependences of the EPC strength of the asymmetric B_{1g} and A_{1g} phonon modes, we fit these two phonon modes using BWF line shapes^[42-43]:

$$I(\omega) = I_0 \frac{\left(1 + \frac{\omega - \omega_{ph}}{q\Gamma}\right)^2}{1 + \left(\frac{\omega - \omega_{ph}}{\Gamma}\right)^2} \quad (3)$$

where I_0 , ω_{ph} , Γ and $1/|q|$ are the maximal intensity, energy, full width at half maxima (i.e., FWHM), and asymmetric factors of the BWF line shapes, respectively (see the fitting parameters at different temperatures in **Table S1** of Supporting Information). The upper and lower panels of **Figure 3a** and **3b** depict the BWF fits to the B_{1g} and A_{1g} phonon modes at two typical temperatures $T = 15$ K and 300 K, respectively. The asymmetric factors (i.e., $1/|q|(B_{1g}, 15 \text{ K}) \sim 0.013$ and $1/|q|(A_{1g}, 15 \text{ K}) \sim 0.012$) for the BWF fits to the B_{1g} and A_{1g} phonon modes at $T = 15$ K is distinctly smaller than those (i.e., $1/|q|(B_{1g}, 300 \text{ K}) \sim 0.075$ and $1/|q|(A_{1g}, 300 \text{ K}) \sim 0.055$) at $T = 300$ K, which suggests that the EPC in EuAl_4 at $T = 15$ K is weaker than that at $T = 300$ K. To get the temperature evolution of the EPC, we plotted the two $1/|q|$ for the B_{1g} and A_{1g} phonon modes in the temperature range from 15 to 300 K in **Figure 3c**. Above T_c , the two $1/|q|$ show weak temperature dependences, but below T_c , the two $1/|q|$ decrease sharply with lowering temperature, which indicates that EPC is weakened after the CDW transition.

Figure 3c displays that the previously reported relative Drude weight $S_D(T)/S_D(300 \text{ K})$ of EuAl_4 which is proportional to the free charge carrier density n_c as a function of temperature^[44]. The significant suppression of the $S_D(T)/S_D(300 \text{ K})$ below T_c manifests that the free charge

carrier density is dramatically lowered after the CDW phase transition in EuAl₄. **Figure 3d** shows that the two $1/|q|$ of the B_{1g} and A_{1g} phonon modes decrease with the lowering of the free charge carrier density, which suggests that the weakening of EPC after the CDW transition in EuAl₄ is likely to be caused by the reduction of the carrier density. In addition, as shown by the dashed line in **Figure 3d**, both the two $1/|q|$ of the B_{1g} and A_{1g} phonon modes below 50 K can be linearly extrapolated to zero at $S_D(T)/S_D(300\text{ K}) = 0$ (see the black dashed line in **Figure 3d**), which implies that in EuAl₄, the vanishing of free charge carriers would make the B_{1g} and A_{1g} phonon modes recover their Lorentzian line shapes with $1/|q| = 0$. Surprisingly, in the temperature from 50 to 145 K, on the right side of the red dashed vertical line in **Figure 3d**, the two $1/|q|$ of the B_{1g} and A_{1g} phonon modes grow steeply and deviate significantly from the linear dependence on the $S_D(T)/S_D(300\text{ K})$. It is well known that the BWF line shapes of the phonon modes in solids arise from the coupling between phonons and electron-hole pair excitations due to EPC^[42-43]. The abrupt growth of the two $1/|q|$ of the B_{1g} and A_{1g} phonon modes with increasing temperature from 50 to 145 K suggests that in EuAl₄, an intermediate electronic state with distinctly larger EPC than the incommensurate CDW ground state may exist in the temperature range 50—145 K, which is supported by the presence of the shoulder-like features around $T \sim 50$ K in the temperature dependences of the $1/|q|$ here (see the purple down arrow in **Figure 3c**). Moreover, if there is no intermediate electronic state in a CDW material, its Drude weight would drop quickly and continuously with the absence of a shoulder-like feature in the temperature dependence of the Drude weight after the CDW phase transition^[45]. However, a shoulder-like feature is present around $T \sim 50$ K in the temperature dependences

of the previously reported $S_D(T)/S_D(300\text{ K})$ (see the red up arrow in **Figure 3c**), which further supports the possible intermediate electronic state in EuAl_4 .

To estimate the evolution of the PPI across the CDW phase transition in EuAl_4 , we studied the temperature evolutions of the FWHMs and energies of its B_{1g} and A_{1g} phonon modes. **Figure 4a** and **4b** show that the FWHM of the B_{1g} phonon mode drops more fastly below T_c than above T_c , while the FWHM of the A_{1g} phonon mode shows unobvious anomaly. Given the anharmonic and harmonic contributions to the FWHMs of the B_{1g} and A_{1g} phonons, the temperature dependence of the FWHM of A_{1g} phonon above and below T_c can be fit well using one PPI parameter ($\lambda_{\text{ph-ph}} \sim 0.38$) in the temperature range 15—300 K based on the following relationship^[21, 46-47]:

$$\Gamma(T) = \Gamma_0 \left[1 + \frac{2\lambda_{\text{ph-ph}}}{\exp\left(\frac{\hbar\omega_0}{2k_B T}\right) - 1} \right] \quad (4)$$

where ω_0 and Γ_0 are the energy and linewidth of phonon at 0 K (see the fitting parameters in **Table S2** of Supporting Information). By contrast, the PPI parameter for fitting the temperature evolution of the B_{1g} phonon FWHM increases from 0.04 to 0.31 upon entering the CDW state (see the fitting parameters in **Table S2**). Considering that the B_{1g} phonon, rather than the A_{1g} phonon, corresponds to the collective vibrations of the Al^1 atoms which are modulated periodically after the CDW transition, the CDW phase transition in EuAl_4 leads to a remarkable growth of the PPI for the B_{1g} phonon below T_c .

To check the enhancement of the phonon-phonon interactions in EuAl₄ after the CDW transition, we plotted the energies of the B_{1g} and A_{1g} phonon modes as a function of temperature in **Figure 4c** and **4d**, respectively. Generally, phonon-mode energy can be given by the following relationships which contain anharmonic ($\omega_{ah}(T)$), quasi-harmonic ($\omega_{qh}(T)$) and harmonic (i.e., ω_h) terms^[21, 46-47]:

$$\omega(T) = \omega_h + \omega_{qh}(T) + \omega_{ah}(T) \quad (5)$$

$$\omega_{ah}(T) = -\omega_0 \left\{ \left(\frac{\Gamma_0}{\sqrt{2}\omega_0} \right)^2 \left[1 + \frac{4\lambda_{ph-ph}}{\exp\left(\frac{\hbar\omega_0}{2k_B T}\right) - 1} \right] \right\} \quad (6)$$

$$\omega_{qh}(T) = \omega_0 \left\{ \exp \left[-3\gamma \int_0^T \alpha_i(T') dT' \right] - 1 \right\} \quad (7)$$

where γ is the Grüneisen parameter of a phonon mode and $\alpha_i(T')$ is the coefficient of the linear thermal expansion at temperature T' . Here, the temperature dependences of the quasi-harmonic terms of the B_{1g} and A_{1g} phonon energies are given by the product of the Grüneisen constant γ and the integral of the linear expansion coefficient up to a temperature T (see the integral of the linear expansion coefficient in Section 2 and **Figure S1** of Supporting Information)^[48]. Therein, the temperature dependence of the linear expansion coefficient of EuAl₄ were obtained by the previously reported thermodynamic investigation. Thus, fitting the temperature dependences of the B_{1g} and A_{1g} phonon energies based on Equation (5)-(7) yields the Grüneisen constants (for the B_{1g} phonon, $\gamma_{B_{1g}} = 1.9$ above T_c and $\gamma_{B_{1g}} = 6.1$ below T_c and for the A_{1g} phonon, $\gamma_{A_{1g}} = 1.8$ above and below T_c) and the PPI parameters (for the B_{1g} phonon, $\lambda_{ph-ph}^{B_{1g}} = 0.04$ above T_c and $\lambda_{ph-ph}^{B_{1g}} = 0.31$ below T_c , while for the A_{1g} phonon, $\lambda_{ph-ph}^{A_{1g}} = 0.38$ above and below T_c), which are consistent with the PPI parameters obtained via fitting the

temperature dependences of the FWHMs of the B_{1g} and A_{1g} phonons based on Equation (4) (see the fitting parameters in **Table S2** of Supporting Information).

It is worth noticing that PPI not only can be mediated by electrons due to EPC^[49] but also can come from lattice anharmonicity^[21, 47, 50]. If the PPI in EuAl_4 are mediated by electrons, the decrease in the EPC strengths estimated from the two $1/|q|$ of the B_{1g} and A_{1g} phonon modes upon entering the CDW state should correspond to the weakening of the PPI. On the contrary, after the CDW phase transition in EuAl_4 , the PPI parameter for the B_{1g} phonon is enhanced from 0.04 to 0.31. Thus, the PPI in EuAl_4 should mainly arise from lattice anharmonicity. Moreover, the remarkable growth of the PPI for the B_{1g} phonon below T_c implies the strengthening of lattice anharmonicity after the CDW phase transition in EuAl_4 .

In summary, using Raman spectroscopy, we have investigated the PPI and EPC in CDW topological semimetal EuAl_4 . Two asymmetric peak-like features in the Raman spectra of the EuAl_4 single crystals are assigned to the Raman-active phonon modes A_{1g} and B_{1g} . Below T_c , the reduction of the Fano asymmetric factors ($1/|q|$) of the two phonon modes A_{1g} and B_{1g} indicates that the EPC becomes weakened after the CDW phase transition. Moreover, the decrease in the Fano asymmetric factors ($1/|q|$) is accompanied with the suppression of free charge carrier density (n_c), which suggests that the weakening of the EPC in EuAl_4 is likely caused by the reduction of the n_c . Unexpectedly, in the temperature range 50—145 K, the two $1/|q|$ grow steeply and deviate significantly from the linear dependences on the n_c . The steep growth of the $1/|q|$, combined with the shoulder-like features in the temperature evolutions of

the $1/|q|$ and the n_c around 50 K, implies the possible existence of an intermediate electronic state with the EPC distinctly larger than the CDW ground state in EuAl₄. Furthermore, the FWHM of the B_{1g} phonon mode representing the collective vibrations of the CDW-modulated Al^I atoms decreases more fastly below T_c than above T_c , which manifests that a remarkable growth of the PPI for the B_{1g} phonon mode after the CDW phase transition. Since the remarkable growth of the PPI for the B_{1g} phonon mode is in contrast to the weakening of the EPC below T_c , the PPI enhancement may mainly originate from the strengthening of lattice anharmonicity in EuAl₄. Our work not only establishes the importance of the enhanced PPI and the weakened EPC for revealing the formation mechanism of the CDW phase but also offers a clue to discovering exotic intermediate electronic states in EuAl₄.

Supporting Information

Single crystals growth, structural characteristics, fitting details about the quasiharmonic and anharmonic models, details about the *ab initio* calculations of the phonon spectrum and fitting parameters for the BWF, quasiharmonic and anharmonic models.

Author Information

Corresponding Authors

Zhi-Guo Chen – Beijing National Laboratory for Condensed Matter Physics, Institute of Physics, Chinese Academy of Sciences, Beijing 100190, China; Email: zgchen@iphy.ac.cn

Yun-Ze Long – Collaborative Innovation Center for Nanomaterials & Devices, College of Physics, Qingdao University, Qingdao 266071, China; Email: yunze.long@qdu.edu.cn

Authors

Shize Cao – Beijing National Laboratory for Condensed Matter Physics, Institute of Physics, Chinese Academy of Sciences, Beijing 100190, China

Feng Jin – Beijing National Laboratory for Condensed Matter Physics, Institute of Physics, Chinese Academy of Sciences, Beijing 100190, China

Jianzhou Zhao – Co-Innovation Center for New Energetic Materials, Southwest University of Science and Technology, Mianyang 621010, China

Jianlin Luo – Beijing National Laboratory for Condensed Matter Physics, Institute of Physics, Chinese Academy of Sciences, Beijing 100190, China

Qingming Zhang – Beijing National Laboratory for Condensed Matter Physics, Institute of Physics, Chinese Academy of Sciences, Beijing 100190, China

Author Contributions

Z.-G.C. conceived and supervised this project; S.C. grew the single crystals; F.J. and Q.Z. built up the Raman measurement system; J.Z. performed the *ab initio* calculations of the phonon spectrum; S.C. carried out the Raman measurements with the assistance of F.J.; Z.-G.C., S.C., Y.L. and J.L. analyzed the data; Z.-G.C. wrote the paper with the input from S.C..

Notes

The authors declare no conflict of interest.

Acknowledgements

The authors acknowledge support from the Guangdong Basic and Applied Basic Research Foundation (Project No. 2021B1515130007), the National Natural Science Foundation of China (Project No. U21A20432 and 12274186), the strategic Priority Research Program of

Chinese Academy of Sciences (Project No. XDB33000000), the National Key Research and Development Program of China (Grant No. 2022YFA1403800, 2024YFA1408301 and 2022YFA1402704) and the Synergetic Extreme Condition User Facility (SECUF, <https://cstr.cn/31123.02.SECUF>).

References:

- [1] A. J. Achkar, M. Zwiebler, C. McMahon, F. He, R. Sutarto, I. Djianto, Z. Hao, M. J. P. Gingras, M. Hücker, G. D. Gu, A. Revcolevschi, H. Zhang, Y. J. Kim, J. Geck, D. G. Hawthorn. Nematicity in stripe-ordered cuprates probed via resonant x-ray scattering. *Science* **2016**, 351 (6273), 576.
- [2] T. Asaba, A. Onishi, Y. Kageyama, T. Kiyosue, K. Ohtsuka, S. Suetsugu, Y. Kohsaka, T. Gagli, Y. Kasahara, H. Murayama, K. Hashimoto, R. Tazai, H. Kontani, B. R. Ortiz, S. D. Wilson, Q. Li, H. H. Wen, T. Shibauchi, Y. Matsuda. Evidence for an odd-parity nematic phase above the charge-density-wave transition in a kagome metal. *Nat. Phys.* **2024**, 20 (1), 40.
- [3] W. Chen, W. Ren, N. Kennedy, M. H. Hamidian, S. Uchida, H. Eisaki, P. D. Johnson, S. M. O'Mahony, J. C. S. Davis. Identification of a nematic pair density wave state in $\text{Bi}_2\text{Sr}_2\text{CaCu}_2\text{O}_{8+x}$. *Proc. Natl. Acad. Sci.* **2022**, 119 (31), e2206481119.
- [4] Z. Jiang, H. Ma, W. Xia, Z. Liu, Q. Xiao, Z. Liu, Y. Yang, J. Ding, Z. Huang, J. Liu, Y. Qiao, J. Liu, Y. Peng, S. Cho, Y. Guo, J. Liu, D. Shen. Observation of Electronic Nematicity Driven by the Three-Dimensional Charge Density Wave in Kagome Lattice KV_3Sb_5 . *Nano Lett.* **2023**, 23 (12), 5625.
- [5] J. Gooth, B. Bradlyn, S. Honnali, C. Schindler, N. Kumar, J. Noky, Y. Qi, C. Shekhar, Y. Sun, Z. Wang, B. A. Bernevig, C. Felser. Axionic charge-density wave in the Weyl semimetal $(\text{TaSe}_4)_2\text{I}$. *Nature* **2019**, 575 (7782), 315.
- [6] Z. Wang, S.-C. Zhang. Chiral anomaly, charge density waves, and axion strings from Weyl semimetals. *Phys. Rev. B* **2013**, 87 (16), 161107.

- [7] A. H. Castro Neto. Charge Density Wave, Superconductivity, and Anomalous Metallic Behavior in 2D Transition Metal Dichalcogenides. *Phys. Rev. Lett.* **2001**, *86* (19), 4382.
- [8] E. Morosan, H. W. Zandbergen, B. S. Dennis, J. W. G. Bos, Y. Onose, T. Klimczuk, A. P. Ramirez, N. P. Ong, R. J. Cava. Superconductivity in Cu_xTiSe_2 . *Nat. Phys.* **2006**, *2* (8), 544.
- [9] B. R. Ortiz, S. M. L. Teicher, Y. Hu, J. L. Zuo, P. M. Sarte, E. C. Schueller, A. M. M. Abeykoon, M. J. Krogstad, S. Rosenkranz, R. Osborn, R. Seshadri, L. Balents, J. He, S. D. Wilson. CsV_3Sb_5 : A Z_2 Topological Kagome Metal with a Superconducting Ground State. *Phys. Rev. Lett.* **2020**, *125* (24), 247002.
- [10] Q. Wang, P. Kong, W. Shi, C. Pei, C. Wen, L. Gao, Y. Zhao, Q. Yin, Y. Wu, G. Li, H. Lei, J. Li, Y. Chen, S. Yan, Y. Qi. Charge Density Wave Orders and Enhanced Superconductivity under Pressure in the Kagome Metal CsV_3Sb_5 . *Adv. Mater.* **2021**, *33* (42), 2102813.
- [11] X. Xi, Z. Wang, W. Zhao, J.-H. Park, K. T. Law, H. Berger, L. Forró, J. Shan, K. F. Mak. Ising pairing in superconducting NbSe_2 atomic layers. *Nat. Phys.* **2016**, *12* (2), 139.
- [12] G. Zheng, C. Tan, Z. Chen, M. Wang, X. Zhu, S. Albarakati, M. Algarni, J. Partridge, L. Farrar, J. Zhou, W. Ning, M. Tian, M. S. Fuhrer, L. Wang. Electrically controlled superconductor-to-failed insulator transition and giant anomalous Hall effect in kagome metal CsV_3Sb_5 nanoflakes. *Nat. Commun.* **2023**, *14* (1), 678.
- [13] Y. Cao, D. Rodan-Legrain, J. M. Park, N. F. Q. Yuan, K. Watanabe, T. Taniguchi, R. M. Fernandes, L. Fu, P. Jarillo-Herrero. Nematicity and competing orders in superconducting magic-angle graphene. *Science* **2021**, *372* (6539), 264.
- [14] R. M. Fernandes, A. J. Millis. Nematicity as a Probe of Superconducting Pairing in Iron-Based Superconductors. *Phys. Rev. Lett.* **2013**, *111* (12), 127001.
- [15] S. Kasahara, H. J. Shi, K. Hashimoto, S. Tonegawa, Y. Mizukami, T. Shibauchi, K. Sugimoto, T. Fukuda, T. Terashima, A. H. Nevidomskyy, Y. Matsuda. Electronic nematicity above the structural and superconducting transition in $\text{BaFe}_2(\text{As}_{1-x}\text{P}_x)_2$. *Nature* **2012**, *486* (7403), 382.
- [16] K. Nakayama, Y. Miyata, G. N. Phan, T. Sato, Y. Tanabe, T. Urata, K. Tanigaki, T. Takahashi. Reconstruction of Band Structure Induced by Electronic Nematicity in an FeSe Superconductor. *Phys. Rev. Lett.* **2014**, *113* (23), 237001.

- [17] T. Shimojima, Y. Motoyui, T. Taniuchi, C. Bareille, S. Onari, H. Kontani, M. Nakajima, S. Kasahara, T. Shibauchi, Y. Matsuda, S. Shin. Discovery of mesoscopic nematicity wave in iron-based superconductors. *Science* **2021**, 373 (6559), 1122.
- [18] Q. Wang, Y. Shen, B. Pan, Y. Hao, M. Ma, F. Zhou, P. Steffens, K. Schmalzl, T. R. Forrester, M. Abdel-Hafiez, X. Chen, D. A. Chareev, A. N. Vasiliev, P. Bourges, Y. Sidis, H. Cao, J. Zhao. Strong interplay between stripe spin fluctuations, nematicity and superconductivity in FeSe. *Nat. Mater.* **2016**, 15 (2), 159.
- [19] J. Lindhard. On the properties of a gas of charged particles. *Kgl. Danske Videnskab. Selskab Mat.-Fys. Medd.* **1954**, 28.
- [20] R. E. Peierls, *Quantum theory of solids*, Clarendon Press, **1964**.
- [21] G. He, L. Peis, E. F. Cuddy, Z. Zhao, D. Li, Y. Zhang, R. Stumberger, B. Moritz, H. Yang, H. Gao, T. P. Devereaux, R. Hackl. Anharmonic strong-coupling effects at the origin of the charge density wave in CsV₃Sb₅. *Nat. Commun.* **2024**, 15 (1), 1895.
- [22] Y. Y. Peng, A. A. Husain, M. Mitrano, S. X. L. Sun, T. A. Johnson, A. V. Zakrzewski, G. J. MacDougall, A. Barbour, I. Jarrige, V. Bisogni, P. Abbamonte. Enhanced Electron-Phonon Coupling for Charge-Density-Wave Formation in La_{1.8-x}Eu_{0.2}Sr_xCuO_{4+δ}. *Phys. Rev. Lett.* **2020**, 125 (9), 097002.
- [23] W. Kohn. Image of the Fermi Surface in the Vibration Spectrum of a Metal. *Phys. Rev. Lett.* **1959**, 2 (9), 393.
- [24] Y. Hu, F. Zheng, X. Ren, J. Feng, Y. Li. Charge density waves and phonon-electron coupling in ZrTe₃. *Phys. Rev. B* **2015**, 91 (14), 144502.
- [25] J. H. Wernick, H. J. Williams, A. C. Gossard. Magnetic and paramagnetic resonance properties of EuAl₄. *J. Phys. Chem. Solids* **1967**, 28 (2), 271.
- [26] S. Araki, Y. Ikeda, T. C. Kobayashi, A. Nakamura, Y. Hiranaka, M. Hedo, T. Nakama, Y. Ōnuki. Charge density wave transition in EuAl₄. *J. Phys. Soc. Jpn.* **2014**, 83 (1), 015001.
- [27] A. Nakamura, Y. Hiranaka, M. Hedo, T. Nakama, Y. Miura, H. Tsutsumi, A. Mori, K. Ishida, K. Mitamura, Y. Hirose, K. Sugiyama, F. Honda, T. Takeuchi, T. D. Matsuda, E. Yamamoto, Y. Haga, Y. nuki, in *JPS Conference Proceedings*, Vol. 3 Journal of the Physical Society of Japan, **2014**.

- [28] A. Nakamura, T. Uejo, F. Honda, T. Takeuchi, H. Harima, E. Yamamoto, Y. Haga, K. Matsubayashi, Y. Uwatoko, M. Hedo. Transport and magnetic properties of EuAl_4 and EuGa_4 . *J. Phys. Soc. Jpn.* **2015**, *84* (12), 124711.
- [29] S. Ramakrishnan, S. R. Kotla, T. Rekiş, J.-K. Bao, C. Eisele, L. Noohinejad, M. Tolkiehn, C. Paulmann, B. Singh, R. Verma. Orthorhombic charge density wave on the tetragonal lattice of EuAl_4 . *IUCrJ* **2022**, *9* (3), 378.
- [30] S. Shimomura, H. Murao, S. Tsutsui, H. Nakao, A. Nakamura, M. Hedo, T. Nakama, Y. Ōnuki. Lattice modulation and structural phase transition in the antiferromagnet EuAl_4 . *J. Phys. Soc. Jpn.* **2019**, *88* (1), 014602.
- [31] H. Miao, J. Bouaziz, G. Fabbris, W. R. Meier, F. Z. Yang, H. X. Li, C. Nelson, E. Vescovo, S. Zhang, A. D. Christianson, H. N. Lee, Y. Zhang, C. D. Batista, S. Blügel. Spontaneous Chirality Flipping in an Orthogonal Spin-Charge Ordered Topological Magnet. *Phys. Rev. X* **2024**, *14* (1), 011053.
- [32] A. M. Vibhakar, D. D. Khalyavin, F. Orlandi, J. M. Moya, S. Lei, E. Morosan, A. Bombardi. Spontaneous reversal of spin chirality and competing phases in the topological magnet EuAl_4 . *Commun. Phys.* **2024**, *7* (1), 313.
- [33] M. Kobata, S.-i. Fujimori, Y. Takeda, T. Okane, Y. Saitoh, K. Kobayashi, H. Yamagami, A. Nakamura, M. Hedo, T. Nakama, Y. Ōnuki. Electronic Structure of EuAl_4 Studied by Photoelectron Spectroscopy. *J. Phys. Soc. Jpn.* **2016**, *85* (9), 094703.
- [34] L.-L. Wang, N. K. Nepal, P. C. Canfield. Origin of charge density wave in topological semimetals SrAl_4 and EuAl_4 . *Commun. Phys.* **2024**, *7* (1), 111.
- [35] R. Takagi, N. Matsuyama, V. Ukleev, L. Yu, J. S. White, S. Francoual, J. R. L. Mardegan, S. Hayami, H. Saito, K. Kaneko, K. Ohishi, Y. Ōnuki, T.-h. Arima, Y. Tokura, T. Nakajima, S. Seki. Square and rhombic lattices of magnetic skyrmions in a centrosymmetric binary compound. *Nat. Commun.* **2022**, *13* (1), 1472.
- [36] T. Shang, Y. Xu, D. J. Gawryluk, J. Z. Ma, T. Shiroka, M. Shi, E. Pomjakushina. Anomalous Hall resistivity and possible topological Hall effect in the EuAl_4 antiferromagnet. *Phys. Rev. B* **2021**, *103* (2), L020405.
- [37] A. N. Korshunov, A. S. Sukhanov, S. Gebel, M. S. Pavlovskii, N. D. Andriushin, Y. Gao, J.

- M. Moya, E. Morosan, M. C. Rahn. Phonon softening and atomic modulations in EuAl_4 . *Phys. Rev. B* **2024**, *110* (4), 045102.
- [38] Y. Chen, L. Wu, H. Xu, C. Cong, S. Li, S. Feng, H. Zhang, C. Zou, J. Shang, S. A. Yang, K. P. Loh, W. Huang, T. Yu. Visualizing the Anomalous Charge Density Wave States in Graphene/ NbSe_2 Heterostructures. *Adv. Mater.* **2020**, *32* (45), 2003746.
- [39] H. Wang, Y. Chen, M. Duchamp, Q. Zeng, X. Wang, S. H. Tsang, H. Li, L. Jing, T. Yu, E. H. T. Teo, Z. Liu. Large-Area Atomic Layers of the Charge-Density-Wave Conductor TiSe_2 . *Adv. Mater.* **2018**, *30* (8), 1704382.
- [40] B. Su, Y. Song, Y. Hou, X. Chen, J. Zhao, Y. Ma, Y. Yang, J. Guo, J. Luo, Z.-G. Chen. Strong and Tunable Electrical Anisotropy in Type-II Weyl Semimetal Candidate WP_2 with Broken Inversion Symmetry. *Adv. Mater.* **2019**, *31* (44), 1903498.
- [41] B. Su, Y. Huang, Y. H. Hou, J. Li, R. Yang, Y. Ma, Y. Yang, G. Zhang, X. Zhou, J. Luo, Z.-G. Chen. Persistence of Monoclinic Crystal Structure in 3D Second-Order Topological Insulator Candidate $1T'$ - MoTe_2 Thin Flake Without Structural Phase Transition. *Adv. Sci.* **2022**, *9* (5), 2101532.
- [42] U. Fano. Effects of Configuration Interaction on Intensities and Phase Shifts. *Phys. Rev.* **1961**, *124* (6), 1866.
- [43] P. Eklund, K. Subbaswamy. Analysis of Breit-Wigner line shapes in the Raman spectra of graphite intercalation compounds. *Phys. Rev. B* **1979**, *20* (12), 5157.
- [44] R. Yang, C. C. Le, P. Zhu, Z. W. Wang, T. Shang, Y. M. Dai, J. P. Hu, M. Dressel. Charge density wave transition in the magnetic topological semimetal EuAl_4 . *Phys. Rev. B* **2024**, *109* (4), L041113.
- [45] Y. Huang, H. P. Wang, R. Y. Chen, X. Zhang, P. Zheng, Y. G. Shi, N. L. Wang. Revealing multiple density wave orders in nonsuperconducting titanium oxypnictide $\text{Na}_2\text{Ti}_2\text{As}_2\text{O}$. *Phys. Rev. B* **2014**, *89* (15), 155120.
- [46] H. M. Eiter, P. Jaschke, R. Hackl, A. Bauer, M. Gangl, C. Pfleiderer. Raman study of the temperature and magnetic-field dependence of the electronic and lattice properties of MnSi . *Phys. Rev. B* **2014**, *90* (2), 024411.
- [47] P. G. Klemens. Anharmonic Decay of Optical Phonons. *Phys. Rev.* **1966**, *148* (2), 845.

- [48]W. R. Meier, J. R. Torres, R. P. Hermann, J. Zhao, B. Lavina, B. C. Sales, A. F. May. Thermodynamic insights into the intricate magnetic phase diagram of EuAl_4 . *Phys. Rev. B* **2022**, *106* (9), 094421.
- [49]D. Novko, M. Alducin, J. I. Juaristi. Electron-Mediated Phonon-Phonon Coupling Drives the Vibrational Relaxation of CO on Cu(100). *Phys. Rev. Lett.* **2018**, *120* (15), 156804.
- [50]N. K. Ravichandran, D. Broido. Phonon-Phonon Interactions in Strongly Bonded Solids: Selection Rules and Higher-Order Processes. *Phys. Rev. X* **2020**, *10* (2), 021063.

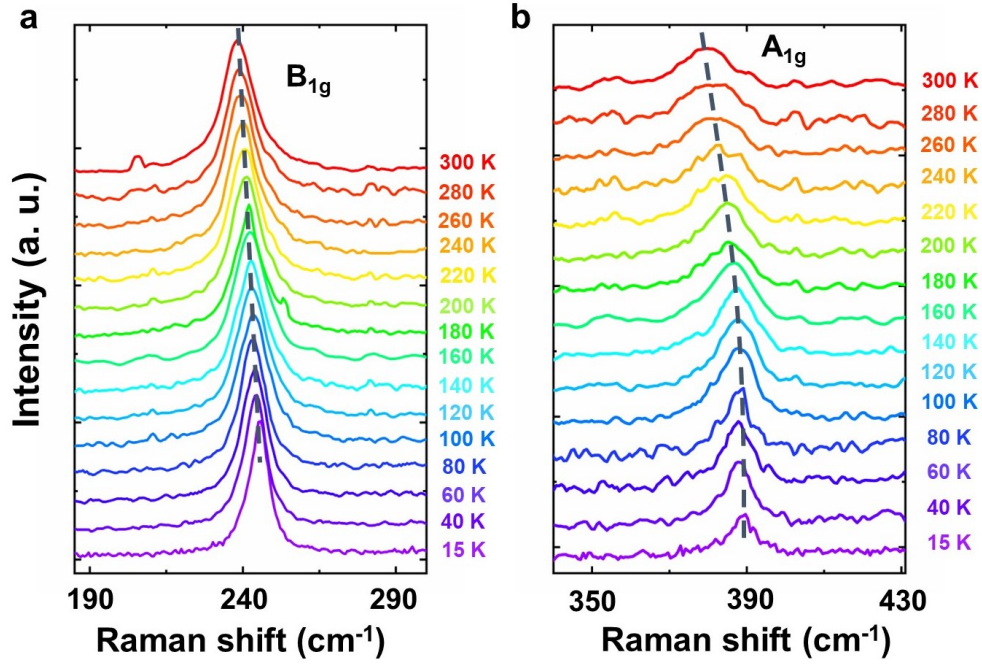


Figure 1. Two asymmetric Raman-active phonon modes B_{1g} and A_{1g} in the Raman spectra of EuAl_4 at different temperatures. The dashed curves in **a)** and **b)** are guides to the eye for the temperature evolutions of the B_{1g} and A_{1g} phonon modes, respectively.

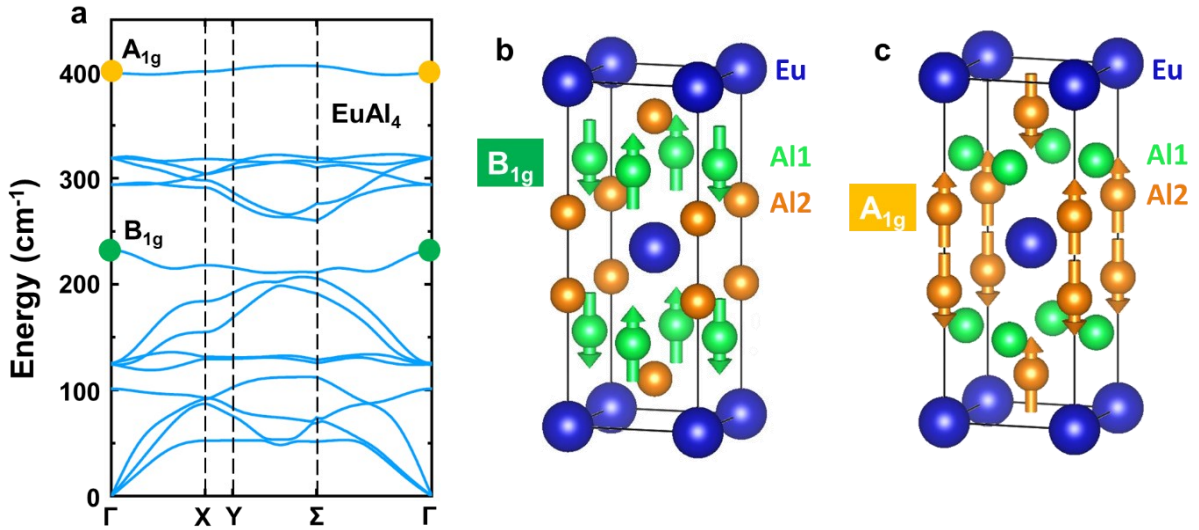


Figure 2. Theoretically calculated Raman-active phonon modes B_{1g} and A_{1g} . **a)** Phonon spectrum of EuAl_4 obtained by *ab initio* calculations. The yellow and green dots in **a)** indicate the calculated energies of the Raman-active phonon modes A_{1g} and B_{1g} . **b)** and **c)** Schematics of the collective vibrations of the Al^1 and Al^2 atoms in EuAl_4 , which separately correspond to the B_{1g} and A_{1g} phonon modes.

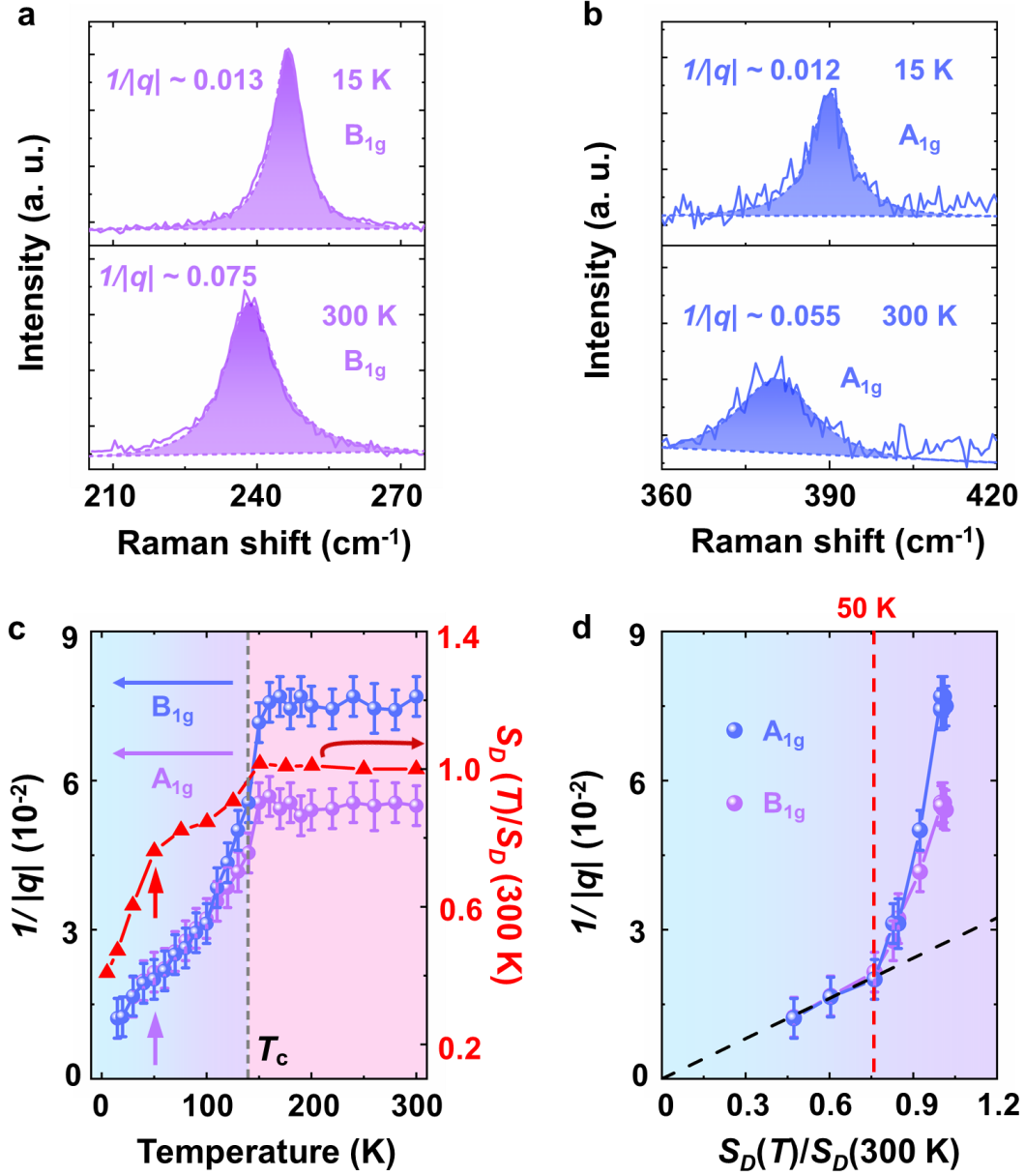


Figure 3. Strength of the Electron-phonon coupling in EuAl₄. **a)** BWF fits to the B_{1g} phonon mode at $T = 15\text{ K}$ and 300 K . **b)** BWF fits to the A_{1g} phonon mode at $T = 15\text{ K}$ and 300 K . **c)** Temperature dependences of the asymmetric factors $1/|q|$ for the B_{1g} and A_{1g} phonon modes and the previously reported relative Drude weight $S_D(T)/S_D(300\text{ K})$. The purple down arrow and the red up arrow in **c)** indicate the shoulder-like features in the temperature dependences of the $1/|q|$ and the $S_D(T)/S_D(300\text{ K})$ around 50 K , respectively. **d)** Two $1/|q|$ of the B_{1g} and A_{1g} phonon modes as a function of the $S_D(T)/S_D(300\text{ K})$. The red dashed vertical line in **d)** shows that on its right side (i.e., in the temperature range $50\text{--}145\text{ K}$), the $1/|q|$ of the B_{1g} and A_{1g} phonon modes grow steeply and deviate significantly from the linear dependence on the $S_D(T)/S_D(300\text{ K})$ (see the black dashed line), which can be linearly extrapolated to zero.

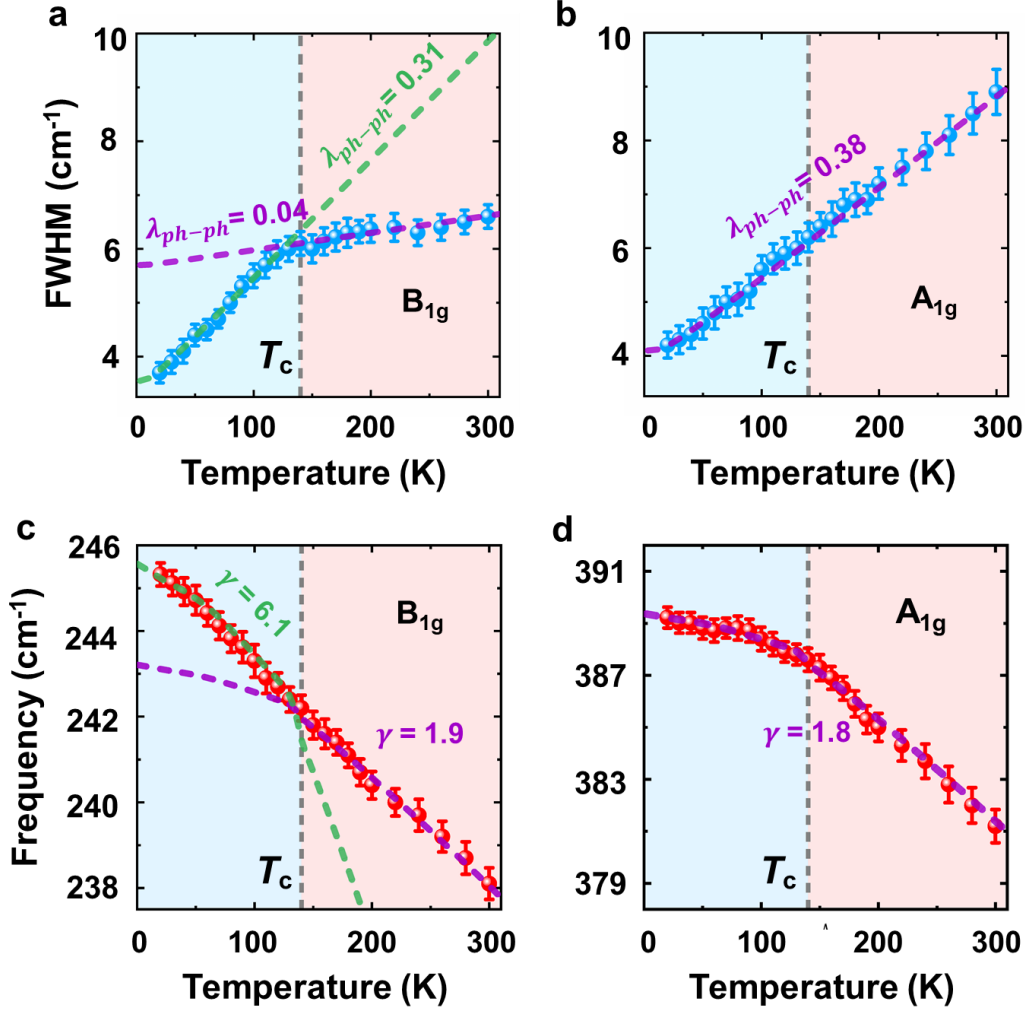


Figure 4. Full widths at half maxima (i.e., FWHMs) and energies of the B_{1g} and A_{1g} phonon modes in the Raman spectra of EuAl_4 as a function of temperature. **a)** Temperature dependence of the FWHM of the B_{1g} phonon mode. The green and purple dashed lines in **a)** shows the fits to the temperature dependence of the FWHM below and above T_c based on Equation (4). The fitting yields the phonon-phonon interaction (PPI) parameters for the B_{1g} phonon mode: $\lambda_{\text{ph-ph}} \sim 0.31$ at $T < T_c$ and $\lambda_{\text{ph-ph}} \sim 0.04$ at $T > T_c$. **b)** Temperature dependence of the FWHM of the A_{1g} phonon mode. The PPI parameter for the A_{1g} phonon mode $\lambda_{\text{ph-ph}} \sim 0.38$ in the temperature range 15–300 K was obtained via the fitting shown by the purple dashed line in **b)**. **c)** Temperature evolution of the B_{1g} phonon energy. The fitting based on Equation (5)-(7) with the PPI parameters for the B_{1g} phonon mode $\lambda_{\text{ph-ph}} \sim 0.04$ and $\lambda_{\text{ph-ph}} \sim 0.31$ yields the Grüneisen parameters $\gamma = 1.9$ at $T > T_c$ and $\gamma = 6.1$ at $T < T_c$, respectively. **d)** Temperature evolution of the A_{1g} phonon energy. The green and purple dashed lines in **a)** shows the fits to the temperature dependence of the A_{1g} phonon energy based on Equation (5)-(7) with $\gamma = 1.8$ and $\lambda_{\text{ph-ph}} \sim 0.38$.

Table 1. Energies of the calculated and measured Raman-active phonon modes B_{1g} and A_{1g} of EuAl_4

Symmetry	Active	Calculated energy [EuAl_4]	Experimental energy [EuAl_4]
A_{1g}	Raman	229.7 cm^{-1}	246 cm^{-1}
B_{1g}	Raman	359.9 cm^{-1}	390 cm^{-1}